Acoustic Transmission Through Compound Subwavelength Slit-Arrays

G. P. Ward, A. P. Hibbins, and J. R. Sambles

Electromagnetic and Acoustic Materials Group, Department of Physics and Astronomy,
University of Exeter, Stocker Road, Devon, EX4 4QL, United Kingdom

J. D. Smith

DSTL, Porton Down, Salisbury, Wiltshire, SP4 0JQ, United Kingdom

The angular dependence of the transmission of sound in air through four types of 2D slit-arrays formed of aluminium slats is explored, both experimentally and numerically. For a simple, subwavelength periodic slit-array, it is well known that Fabry-Perot-like wave-guide resonances, supported by the slit-cavities, hybridising with bound acoustic surface waves, result in 'Enhanced Acoustic Transmission' at frequencies determined by the length, width and separation of each slit-cavity. We demonstrate that altering the spacing or width of some of the slits to form a compound array (i.e. an array having a basis comprised of more than one slit) results in sharp dips in the transmission spectra, that may have a strong angular dependence. These features correspond to 'phase resonances', which have been studied extensively in the electromagnetic case. This geometry allows for additional near-field configurations compared to the simple array, whereby the field in adjacent cavities can be out-of-phase. Several types of compound slit-array are investigated; one such structure is optimised to minimise the effect of boundary-layer loss mechanisms present in each slit cavity, thereby achieving a deep, sharp transmission minimum in a broad maximum.

The experimental discovery of Extraordinary Optical Transmission (EOT) through subwavelength hole arrays[1] opened a whole new area of research into how structured resonant layers can affect the propagation of light. This research has been extended to the acoustic case, where similar behaviour is observed, sometimes termed Enhanced Acoustic Transmission (EAT) (Not extraordinary, since longitudinal sound waves have no cut-off when propagating through gaps/holes in rigid bodies with sound hard walls)[2–7]. The observed phenomena for both electromagnetic and acoustic cases in such structures is due to complex interplay between surface-wave modes and wave-guide modes, the exact nature being dependent on many structural parameters[6–8]. Other types of transmission anomaly have been discovered in the electromagnetic case that stem from EOT. One such anomaly is the 'Phase resonance', which appears as a sharp dip in the transmission of transverse magnetic polarised light through so called 'compound grating' structures, gratings with structure factor comprised of multiple elements[9–14]. In the case of a 2D metal slit-array this can be achieved by having unequally sized slits, or multiple slits in each period. In a singularly periodic grating structure, symmetry requires that the fields in all slit-cavities are identical when excited by a normally incident planar wave. Compound gratings introduce new degrees of freedom to the near field configurations, and at specific frequencies fields in adjacent cavities may be both out-of-phase with one another and strongly enhanced[10], leading to 'phase-resonant' features in their electromagnetic response. Being simply a lattice/symmetry phenomena, there is an expectation that these phase reso-
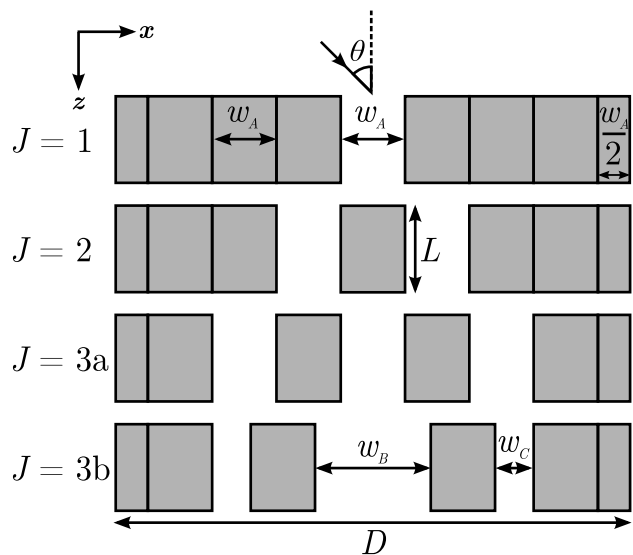

FIG. 1. Schematic of a unit cell of each array sample (not to scale). The grey blocks represent the aluminium slats that form the sample, of width $w_A = 2.9$ mm, and length $L = 19.8$ mm. The air gaps that form the cavities are the same size as the slats, except for the $J = 3b$ sample, where the central cavity w_B has width 5.9 mm, and the outer two have $w_C = 1.5$ mm. Each sample has a period $D = 8w_A = 23.2$ mm.

nances will also exist in the acoustic case[15–17].

Here, we experimentally demonstrate the existence of the airborne acoustic phase resonance with a compound slit-array grating, finding good agreement with numerical model predictions. We also optimise the grating structure to achieve the strongest possible coupling to the phase resonance, with viscous and thermal boundary
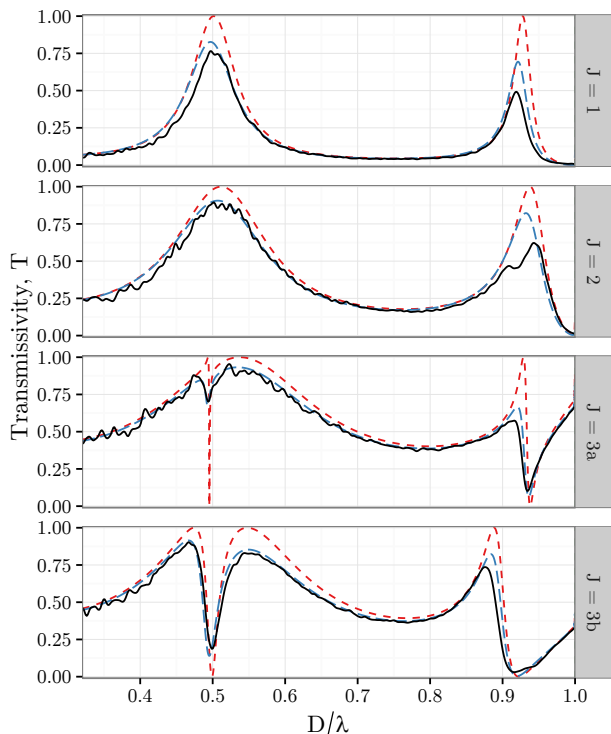
FIG. 3. FEM simulations of the instantaneous pressure fields Δp corresponding to the three available Eigenmodes '$+++$', '$+-+$', and '$+\,0-$', of the $J=3a$ system, exited at normal incidence ($\theta=0$), shown at a temporal phase corresponding to maximum field amplitude. The colour scales have been normalised with normalisation constants 2.19, 4.01 and 3.39 respectively. The three Eigenmodes have resonant frequencies which correspond to $\frac{D}{\lambda}$ values of 0.54, 0.5 and 0.48 respectively. These were calculated using a loss-free FEM model. The grey blocks represent the aluminium slats, in the same orientation as illustrated in figure 1.

.

FIG. 2. Normal incidence transmissivity spectra as a function of the ratio of array periodicity D to incident radiation wavelength λ for each of the sample types illustrated in figure 1. The solid black line is the experimental data, the short-dashed red and long-dashed blue lines are the lossless and viscous-thermal loss-including numerical model spectra for comparison. The diffraction edge for each experimental sample occurs when $\frac{D}{\lambda}=1$. Fluctuations in the ambient temperature are accounted for in the calculation of λ.

layer effects being accounted for.

The experimental samples are illustrated in figure 1. J denotes the number of slits per grating period, with $J=3a$ and $J=3b$ having the same number of slits but with different slit-width ratios. Such gratings are formed of aluminium slats of size 600 mm $\times$ 2.9 mm $\times$ 19.8 mm, stacked in a wooden sample holder, with small polyester spacers used to create the appropriately sized air gaps. The total sample area is 560 mm $\times$ 400 mm, and it is placed with the slats vertical, on a rotating table, symmetrically situated between two spherical mirrors 3 m apart, of radius 220 mm and focal length 1 m. One mirror collimates the sound of a speaker placed at its focal point, directed so that the beam is normal to the face of the slit cavities when the rotating table is set to $\theta=0°$ (normal incidence) producing a beam width smaller than the sample face to approximate an infinite sample size. The other mirror focuses the beam transmitted through the sample on to a Brüel and Kjær 4190 microphone. The speaker is driven by a signal generator producing a Gaussian pulse centred on 8 kHz, containing a broad range of audible frequencies. The sample is ro-
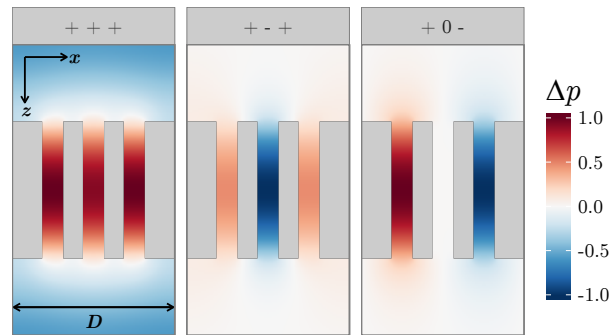
tated between $-2.5°\leq\theta\leq65°$ (limited by the sample size and frame), and the averaged time-domain signal from multiple pulses of the speaker for each angle is recorded by a PC-based oscilloscope. To account for small leakage of the signal around the sample, a large sound opaque slab with anti-reflection absorber foam attached is placed on the incident side of the source. Transmission measurements are then repeated for all angles, and the resulting data subtracted from the original sample data in the time-domain spectra, leaving only the signal transmitted through the sample holder. This is then Fourier analysed to obtain the angular dependent frequency response of the sample. A reference spectrum for each angle is obtained by repeating the experiment with only the wooden sample frame in place, and used to normalise the transmitted signal in the frequency domain.

Figure 2 shows the transmissivity spectra for each sample when probed at normal incidence, as a function of the ratio of array periodicity D to incident wavelength of radiation λ. Also included are the predicted spectra calculated using a Finite-Element-Method (FEM). The red dashed line is the result obtained from the model solving the lossless acoustic wave equation, while the blue long-dashed line comes from a model which solves the linearised Navier-Stokes equation, accounting for viscous and thermal boundary layer effects at each rigid, sound-hard wall[18]. The position of the onset of diffraction corresponds to $\frac{D}{\lambda}=1$. The calculated incident wavelength for each sample takes into account changes in ambient temperature between measurements, acting to vary the speed of sound in air c. Atmospheric pressure and
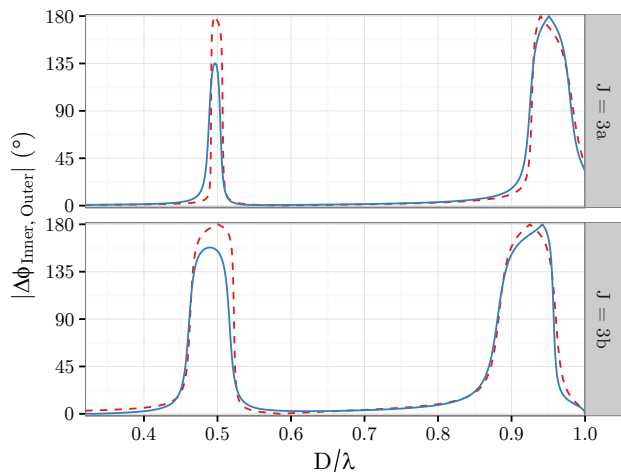
FIG. 4.   Lossless (dotted red line) and viscous-thermal (solid blue line) FEM models of the difference in the phase $|\Delta\phi_{\text{Inner, Outer}}|$ of the tangential particle velocity V_{x} of the central and outer cavities, for the $J = 3a$ and $J = 3b$ samples, plotted as a function of the ratio of array periodicity to incident wavelength $\frac{D}{\lambda}$. The predicted diffraction edge is at $\frac{D}{\lambda} = 1$. Phases were evaluated in the centre of each cavity on the transmitting side of the grating.

humidity changes have negligible effect[19].

It is well known that sound incident on an air cavity bounded by two parallel, infinitely wide, rigid-solid walls of length L will have a broad transmission peak at a frequency naïvely predicted by the Fabry-Perot condition, $f_{\text{FP}} = \frac{nc}{2L}$, where c is the speed of sound and n is an integer. There is a correction ΔL, that takes into account end effects at the exit/entrance of each cavity, which to first order is approximated by $\Delta L = \frac{8w}{3\pi}$, w being the width of the slit[20]. When such cavities are placed in an equally spaced array of period D, such as in sample $J = 1$, the coherent effect of these diffractive waves along the surface of the grating results in a collective resonance, labelled a 'Spoof-Acoustic-Surface-Wave' (SASW). The enhanced fields associated with the SASW on each face of the array couple together via the FP like modes in the slit-cavities. This is the mechanism by which EAT can occur at specific frequencies, resulting in large peaks in the transmission spectrum of such a grating. Indeed, figure 2 shows two broad peaks in the $J = 1$ spectrum, at $\frac{D}{\lambda} = 0.5$ and 0.92. These correspond to the first and second order FP like modes, with the frequency of the $n = 2$ mode perturbed by the strong evanescent diffracted fields near the onset of diffraction. This mechanism has been studied extensively in the past decade[5–7].

The transmission spectrum of the $J = 2$ sample is little different, except for a slight broadening of the FP modes and a small upward frequency shift due to a reduction in the strength of the Fourier amplitude component of the grating profile that causes first order scattering. For the $J = 3$ samples, as well as further broadening of the FP

like modes, a new feature, the 'phase-resonance', appears in the low frequency wing of each primary resonance. As described in the electromagnetic case by both Skigin et al.[10] and Hibbins et al.[12], this is because there is a new degree of freedom in the system. In the $J = 1$ and $J = 2$ cases, the fields in each adjacent cavity must have identical phase at normal incidence, hence an incident planar wave cannot excite a phase resonance. However, with three cavities per period, the outer two slits have different surroundings to the central one. Hence, by symmetry, two field configurations can now be excited at normal incidence; all of the fields in-phase (labelled the '+ + +' mode), and the central and outer cavity fields out-of-phase (the '+ − +' mode, where '−' corresponds to a phase shift of π relative to '+'). This is illustrated in both figures 3 and 4.

Figure 3 shows the instantaneous pressure field of the Eigenmodes of the $J = 3a$ system at normal incidence, calculated with the lossless FEM model, and normalised to their maximum amplitude of Δp, different for each mode. The mode labelled '+ + +' corresponds to the primary resonance at $\frac{D}{\lambda} = 0.53$, where all of the cavities are resonating in-phase, with similar amplitude. This mode is highly radiative and results in the broad transmission peak, with the maximum absolute pressure amplitude within the slits being 3.1 greater than in the incident wave. The second panel, with the mode labelled '+ − +', illustrates the phase resonance Eigenmode that is excitable at normal incidence. The outer two cavities are oscillating exactly π out of phase with the central one, which, as the colour scale shows, has a greater field amplitude. Note, the maximum absolute pressure field amplitude within the cavities has now become 55.7 times greater than in the incident wave, a significant increase compared to the '+ + +' mode, indicating a stronger degree of localisation. Another interesting feature is the apparent standing wave that has formed across the $\boldsymbol{x}$ direction, seen from looking at just the top or bottom of the slits - the cavity resonances appear to be coupled with each other. There is a third field configuration available in the form of the anti-symmetric '+ 0 −' mode, where the outer two cavities are π radians out-of-phase with each other, and $\pi/2$ radians out-of-phase with the central cavity, having no mode amplitude. The $J = 2$ configuration supports a similar '+−' mode, but in neither configuration are these modes excitable at normal incidence, as they require a phase-change along the surface (Incidentally, a weak feature has appeared in the experimental data for the $J = 2$ sample as the collimating mirror does not produce a perfect planar wave, and allows weak coupling to this mode). Direct coupling to any of the phase resonant configurations is impossible as the pressure field within the slit cavities is out of phase with the incident field. Hence, they can only be excited via coupling between slits, and appear as sharp dips in transmission, sat in the primary '+ + +' resonance peak.
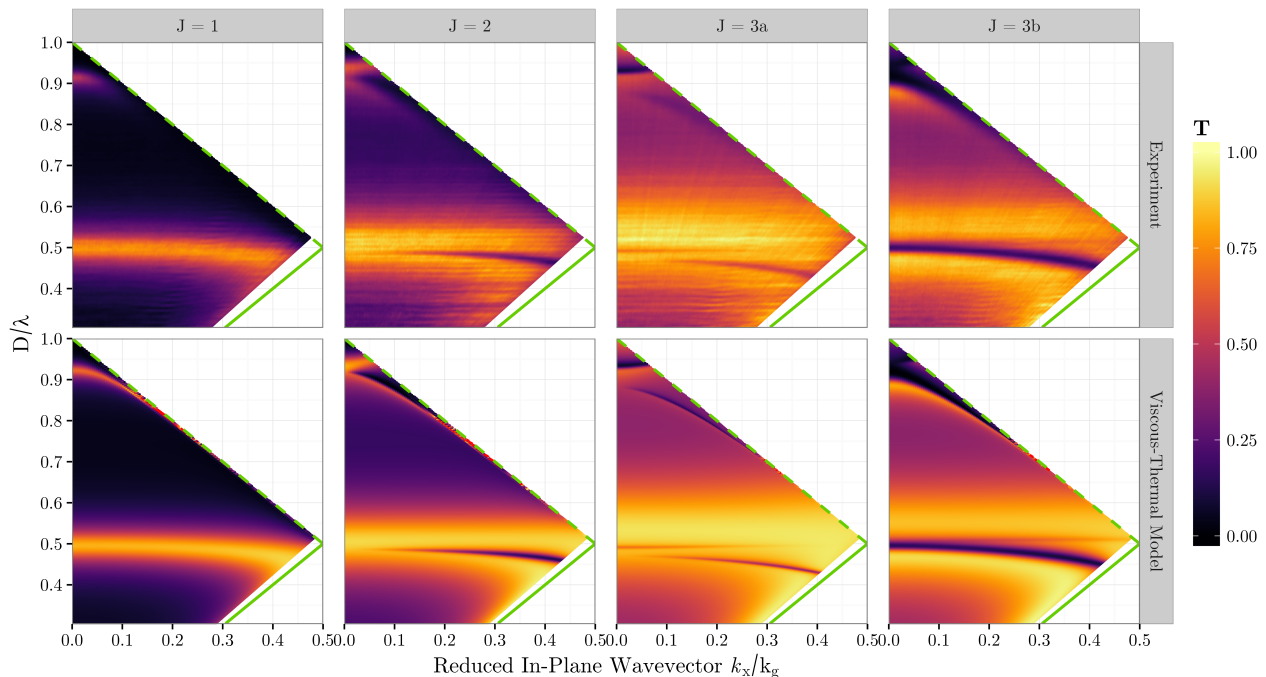
FIG. 5. Transmission data illustrating mode dispersion for each sample illustrated in figure 1, labelled accordingly. The ratio of array periodicity to incident wavelength $\frac{D}{\lambda}$ is plotted as a function of reduced in-plane wavevector $\frac{k_x}{k_g}$, where a value of $\frac{k_x}{k_g} = 0.5$ corresponds to the first Brillouin zone boundary. The top row are the recorded experimental data, whereas the bottom row are the numerical results calculated by the viscous-thermal loss inclusive FEM model. For reference, a solid green line representing grazing incidence k_0 is included on each plot. The onset of first order diffraction is represented by the green dashed line. Fluctuations in ambient room temperature are accounted for in all calculations of λ.

Another way of illustrating the phase resonance is shown in figure 4, which is a plot of the numerically calculated phase difference $|\Delta\phi_{\text{Inner, Outer}}|$ of the velocity field V_x between the central and outer slits, evaluated at the mid-width of the transmitting side of each slit cavity. The structure was excited by a normally incident planar wave, with varying frequency. For both $J = 3a$ and $J = 3b$ samples, at frequencies corresponding to the position of the transmission dips in figure 2, the lossless acoustic wave equation model (red dashed line) predicts a π phase difference between the slits, while away from these resonances and below the onset of diffraction, $|\Delta\phi_{\text{Inner, Outer}}|$ is close to zero.

To obtain the strongest possible reduction in transmission at the phase resonant frequency, there must be perfect balance between the radiative and non-radiative losses in the system. This is the well known 'critical coupling condition'. Non-radiative thermodynamic loss effects form a part of this balance and thus must be accounted for. With sample $J = 3a$, the '+ − +' resonance is a weak feature in the experiment, only reducing transmission by 15% at $\frac{D}{\lambda} = 0.49$, being much stronger in the second order mode ($\frac{D}{\lambda} = 0.94$), reaching a reduction of $\sim 50\%$. The lossless FEM model, solving the acoustic wave equation, predicts a very sharp,

100% deep resonance at $\frac{D}{\lambda} = 0.49$ in the transmission spectrum. However, when viscous-thermal contributions are included (via solving of the linearised Navier-Stokes equation) - which results in a much better agreement with the experimental data - this resonance is significantly more damped. The effect stems from the viscous-thermal boundary layers at the rigid, sound-hard walls, that cause significant attenuation of the fields within the slit-cavities[18]. Note, we have checked that a simpler model that includes only a bulk loss term added to the free space acoustic wave equation does not predict the increased damping effect.

Sample $J = 3b$ is optimised geometrically to balance the radiative and non-radiative loss effects as close to critical coupling as possible while keeping periodicity and slat size constant. This grating is a simple modification of the $J = 3a$ sample, with an inner-cavity-to-outer-cavity ratio of around four-to-one. As figure 2 shows, the experimental data exhibits a much deeper, broader phase resonance in both the fundamental and second order modes. Figure 4 gives extra insight into this phenomenon, showing that the loss inclusive model for the $J = 3a$ sample predicts a maximum $|\Delta\phi_{\text{Inner, Outer}}|$ of $\sim 0.75\pi$ radians at the occurrence of the phase resonance, while it reaches $\sim 0.9\pi$ radians for the optimised $J = 3b$ sample, thus
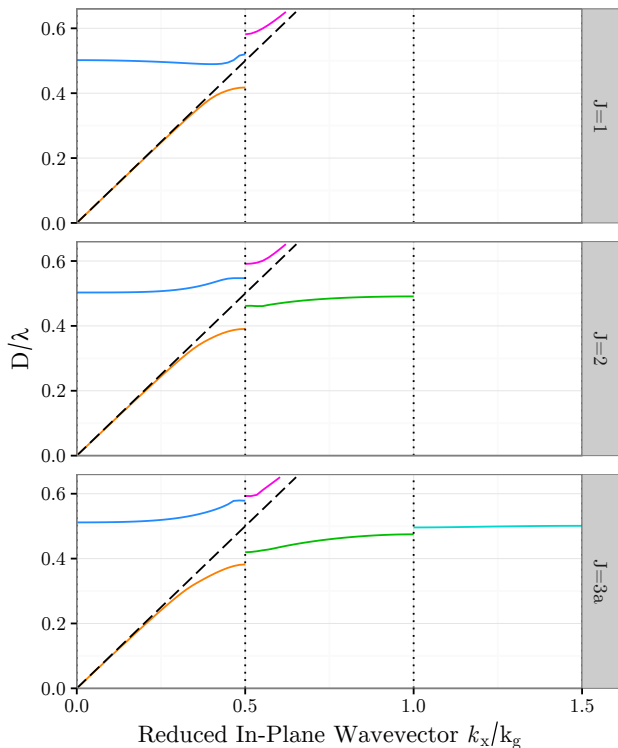
FIG. 6. Dispersion diagrams showing the extended zone scheme representation of the Eigenmodes of the $J = 1$, $J = 2$ and $J = 3a$ systems (all labelled), plotted as a function of the ratio of array periodicity to incident wavelength $\frac{D}{\lambda}$ vs reduced in-plane wave vector $\frac{k_x}{k_g}$. Individual Eigenfrequencies were calculated using loss-free FEM models. The sound line k_0 is represented by the black dashed line. Integer and half integer values of $\frac{k_x}{k_g}$ correspond to different Brillouin zone boundaries, which have been marked with vertical black dotted lines. The solid lines represent the different Eigenmodes supported by each grating structure, with colours signifying different field configurations. Blue is the naturally radiative Fabry-Perot like mode, with pink being it's band split pair. Orange is the non-radiative low frequency SASW, green is the SASW coupled to the low energy phase resonance, and cyan is the SASW coupled to the high energy phase resonance.

displaying stronger coupling to the '$+ - +$' Eigenmode.

By recording angle (θ) dependent data, we map the dispersion and attain a greater understanding of the origin of these modes. Figure 5 shows the transmissivity of each grating as a function of the ratio of incident wavelength to array periodicity, and reduced in-plane wave vector $\frac{k_x}{k_g}$, where $k_x = k_0 \sin \theta$ and $k_g = \frac{2\pi}{D}$.

The simple $J = 1$ grating exhibits a fundamental mode that is largely flat-banded, being strongly localized in the slit-cavity with FP-like fields, where the cavity's length L and width w_A are the dominant variables in determining the resonance position. This mode starts from the FP frequency at $k_x = 0$, and only becomes perturbed as the diffracted sound line from $k_x = k_g$ is approached. There is similar perturbation of the second order mode

$(\frac{D}{\lambda} = 0.9)$.

Additional transmission dips become apparent in the response of the $J = 2, 3a$ and $3b$ samples at $\frac{D}{\lambda} = 0.5$ and $0.1 \leq \frac{k_x}{k_g} \leq 0.4$. These are the anti-symmetric phase resonances that can now be excited with the addition of a phase difference along the grating surface[11, 12], associated with $\theta \neq 0$. For $J = 2$, at high k_x it is now possible to excite the '$+ -$' mode, were the two cavities are π radians out-of-phase. The $J = 3a$ and $J = 3b$ samples also exhibit the additional feature, which has appeared on the low frequency wing of the FP resonance at $\frac{D}{\lambda} = 0.5$. This corresponds to the anti-symmetric '$+ \ 0 \ -$' phase resonance shown in figure 3. In all cases, one can see that at least one of the phase resonances has a strong k_x dependence, indicating that they are surface-wave-like in character. It is possible to deploy a surface-wave band-folding picture to explain the dispersion relations in figure 5. To understand this it is helpful to plot the band-structure of each sample using the extended zone scheme representation, i.e., by drawing the band-structure without band-folding present. This is illustrated in figure 6.

Adding structure factor to each grating periodicity opens up new degrees of freedom to the system, and allows coupling of the phase-resonant near-field configurations to diffracted fields (SASWs) that originate from the diffractive end effects. Figure 6 is a plot of the underlying band structure of the Eigenmodes of the $J = 1$, $J = 2$ and $J = 3a$ samples, in the form of a dispersion diagram with the same axes as those in figure 5. The Eigenfrequencies were calculated using the loss-free FEM model.

With one cavity per unit cell, the $J = 1$ configuration has only two modes available (considering only first order harmonics); the naturally radiative primary FP-like resonance (denoted by the solid blue line) and the low frequency SASW (denoted by the solid orange line) that is only accessible in the non radiative regime as it has in-plane-wavevector $k_x > k_0$. Here, k_0 is represented by the black dashed line, i.e. the 'sound line'. This is the wavevector that a grazing incidence pressure wave would possess. Since this structure only has one cavity per unit cell, and the sample walls can be treated as perfectly rigid, the only degree of freedom available to the near-field is the cavity being either a positive or negative anti-node. This means that any mode which has a shorter surface wavelength than the spacing of the cavities D **cannot** exist, as they must require a pressure field maximum within the rigid walls. Thus, beyond the first Brillouin zone at $k_x = \frac{k_g}{2}$, the SASW ceases to exist - at normal incidence, with band-folding (where the grating periodicity k_g can be added or subtracted to any mode, thereby scattering non-radiative modes into the radiative regime), we will only see the primary FP-like mode.

When there are two cavities per unit cell (sample $J = 2$), there is another possible field configuration apart from the FP like '$+ +$' mode. The adjacent cavities can now
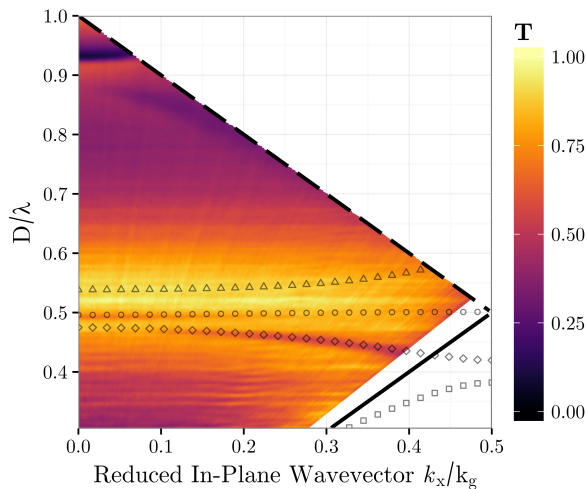
FIG. 7. Dispersion diagram showing the experimental transmissivity T data for the $J = 3a$ sample, with its numerically calculated Eigenfrequencies overlaid, plotted as a function of the ratio of array periodicity to incident wavelength $\frac{D}{\lambda}$ vs reduced in-plane wave vector $\frac{k_x}{k_g}$. The value of $\frac{k_x}{k_g} = 0.5$ corresponds to the first Brillouin zone boundary. The solid black line represents the wavevector k_0 of a grazing incidence pressure wave. The onset of first order diffraction is represented by the black dashed line, being $\frac{D}{\lambda} = 1$ at normal incidence ($\frac{k_x}{k_g} = 0$). The hollow points represent the different Eigenmodes supported by the $J = 3a$ grating structure, with shapes signifying different field configurations. The triangles are the naturally radiative Fabry-Perot like mode, circles are the SASW coupled to the '$+ - +$' phase resonance and the diamonds are the SASW coupled to the '$+ 0 -$' phase resonance. The squares are the non-radiative low frequency SASW which cannot be seen in this transmission experiment.

oscillate π radians out of phase with each other, creating the anti-symmetric '$+ -$' phase resonance. Now, it is possible for a SASW with a shorter wavelength than D to exist, since the extra anti-node per unit cell it requires can now be satisfied. Thus, the low frequency SASW which previously vanished above $k_x = \frac{k_g}{2}$ now band-splits at this first Brillouin zone, and continues up to the next at $k_x = k_g$. This mode is represented by the green line in figure 6, and is band-folded back into the radiative regime by first order scattering from k_g, forming the deep, sharp resonance in our experimental data for the $J = 2$ sample at high k_x. Above $k_x = k_g$, the SASW again ceases to exist; as before, it requires another anti-node per unit cell, and this is forbidden by the lack of a possible near field configuration.

Finally, by increasing the number of cavities per unit cell to three (sample $J = 3a$), yet another degree of freedom is available to the near field. There is now the primary '$+ + +$' configuration, the '$+ - +$' π mode, and the '$+ 0 -$' anti-symmetric mode. Thus, the three-anti-nodes-per-unit-cell condition required for wave-vectors larger than $k_x = k_g$ is satisfied, the SASW band-splits

at $k_x = k_g$ and extends to the next Brillouin zone at $k_x = \frac{3k_g}{2}$, where the same pattern repeats, and beyond this the mode ceases to exist. The second order scattering at $k_x = 2k_g$ band-folds this SASW back into the radiative regime, resulting in the two sharp dips seen in the experimental dispersion data for the $J = 3a$ sample (the band structure for the $J = 3b$ sample is identical in shape since it has the same number of cavities per unit cell, only the coupling strengths and frequencies have changed). This is illustrated in figure 7, where the band-folded Eigenmodes calculated using the loss free FEM model are overlaid onto the $J = 3a$ experimental transmission data. One can see that the dips in transmissivity correspond to the diffracted SASWs. Using this band-folding picture it is easy to see that every time one adds an air cavity to the unit cell, a new degree of freedom is available to the near field, hence a shorter wavelength SASW is able to be band-folded back into the radiative regime, resulting in the appearance of a sharp dip in the transmission spectrum.

It is important to note that the frequency ordering of the modes is not fixed at normal incidence. This is demonstrated by a further change in behaviour visible between the $J = 3a$ and $J = 3b$ samples in figure 5. For the identical width cavity $J = 3a$ case, one can see that the '$+ 0 -$' mode that is not excitable at normal incidence is occupied by the low energy band with high curvature, while the '$+ - +$' configuration is coupled to the high energy flat-banded mode. When the central slit is widened to create the $J = 3b$ sample, this behaviour is reversed, and now the low energy band is excitable at normal incidence. This is because widening the central cavity has redistributed the energies of the SASWs coupling to the '$+-+$' configuration and the '$+ 0 -$' configuration, where the '$+ 0 -$' SASW now has the greater energy of the two, and is at a higher frequency. Note that at the first Brillouin zone, the π phase shift between unit cells requires that the '$+ - +$' configuration always occurs at a higher frequency than the '$+ 0 -$' configuration. Also note that in the $J = 3b$ sample, the '$+ 0 -$' mode is significantly weaker than it was for the $J = 3a$ configuration; narrowing the cavities to 1.5 mm has both increased the quality factor of the mode and increased the relative size of the viscous and thermal boundary layers, leading to significant attenuation[18].

We have checked that it is possible to pull the frequency of the primary '$+ + +$' mode down below the '$+ - +$' and '$+ 0 -$' phase resonances by heavily perturbing the grating structure, so that the two inner rigid slats are very thin and thus the three cavities are very closely spaced (with periodicity constant). This increases the coupling strength between cavities, so that they begin to behave as a single wide cavity, thus increasing length correction ΔL, thereby reducing the resonant frequency. This also increases the strength of the first order scattering Fourier component, again acting to reduce the

resonant frequency. The phase resonances are simultaneously pushed to a higher frequency; the phase shift between cavities has to occur over a shorter distance in x, increasing their energy as before.

In conclusion, we have experimentally and numerically demonstrated the existence of the acoustic phase resonance phenomenon, by studying the transmission of sound through a 2D array of airborne metal slits arranged in four separate configurations. We find that increasing the number of cavity slits per array period, while keeping that period constant, opens up new degrees of freedom to the near field. As well as the standard hybridisation of the Fabry-Perot modes with spoof-acoustic-surface-waves that result in broad transmission peaks, we find dips in the normal incidence transmission spectra that appear when there are three cavities per grating period, being the 'phase-resonant' modes. We also map out the transmission of these structures as a function of incident angle θ, and find that extra field configurations can be excited with the addition of a phase change across the grating surface, for any sample that has more than one slit per period. With this information we describe the origin of each feature with a surface-wave band-folding picture; each mode is a diffractively coupled spoof-acoustic-surface-wave which can be excited via the new field configurations. Finally, we demonstrate the importance of including thermodynamic loss effects when modelling this sort of structure. We optimize one of our samples taking attenuation by viscous and thermal boundary layer effects into account, resulting in measured broad and deep phase resonances that could be useful for the design of acoustic filters.

———————————

[1] T. Ebbesen, H. Lezec, H. F. Ghaemi, T. Thio, and P. Wolff, Nature (London) **391**, 667 (1998).

[2] X. Zhang, Phys. Rev. B **71**, 241102 (2005).

[3] L. Zhou and G. A. Kriegsmann, J. Acoust. Soc. Am. **121**, 3288 (2007).

[4] B. Hou, J. Mei, M. Ke, W. Wen, Z. Liu, J. Shi, and P. Sheng, Phys. Rev. B **76**, 054303 (2007).

[5] M. H. Lu, X. K. Liu, L. Feng, J. Li, C. P. Huang, Y. F. Chen, Y. Y. Zhu, S. N. Zhu, and N. B. Ming, Phys. Rev. Lett. **99**, 174301 (2007).

[6] J. Christensen, L. Martin-Moreno, and F. J. Garcia-Vidal, Phys. Rev. Lett. **101**, 014301 (2008).

[7] X. Wang, J. Appl. Phys. **108**, 064903 (2010).

[8] L. Martín-Moreno, F. J. García-Vidal, H. J. Lezec, K. M. Pellerin, T. Thio, J. B. Pendry, and T. W. Ebbesen, Phys. Rev. Lett. **86**, 1114 (2001), 0008204.

[9] A. N. Fantino, S. I. Grosz, and D. C. Skigin, Phys. Rev. E **64**, 016605 (2001).

[10] D. C. Skigin and R. A. Depine, Phys. Rev. Lett. **95**, 217402 (2005).

[11] D. C. Skigin and R. A. Depine, Phys. Rev. E **74**, 046606 (2006).

[12] A. P. Hibbins, I. R. Hooper, M. J. Lockyear, and J. R. Sambles, Phys. Rev. Lett. **96**, 257402 (2006).

[13] D. C. Skigin, H. Loui, Z. Popovic, and E. F. Kuester, Phys. Rev. E **76**, 016604 (2007), 0702207 [physics].

[14] H. J. Rance, O. K. Hamilton, J. R. Sambles, and A. P. Hibbins, Appl. Phys. Lett. **95**, 041905 (2009).

[15] Z. Liu and G. Jin, J. Phys. Condens. Matter **21**, 445401 (2009).

[16] H. Estrada, V. Gómez-Lozano, A. Uris, P. Candelas, F. Belmar, and F. Meseguer, J. Phys. Condens. Matter **23**, 135401 (2011).

[17] H. Zhang, L. Fan, J. Qu, and S. Zhang, J. Appl. Phys. **119**, 084902 (2016).

[18] G. P. Ward, R. K. Lovelock, A. R. J. Murray, A. P. Hibbins, J. R. Sambles, and J. D. Smith, Phys. Rev. Lett. **115**, 044302 (2015).

[19] O. Cramer, J. Acoust. Soc. Am **93**, 2510 (1993).

[20] L. E. Kinsler, A. R. Frey, A. B. Coppens, and J. V. Sanders, *Fundamentals of Acoustics*, 4th ed., Vol. 1 (John Wiley & Sons, Inc., New York, 1999) p. 274.